AIAA SciTech Forum
23-27 January 2023, National Harbor, MD & Online
AIAA SCITECH 2023 Forum

10.2514/6.2023-0077

Resolvent-based estimation of laminar flow around an airfoil

Junoh Jung*, Rutvij Bhagwat† and Aaron Towne ‡
Department of Mechanical Engineering, University of Michigan, Ann Arbor, MI, USA

We use a resolvent-based approach, recently developed by Martini *et al.* (*J. Fluid Mech.*, vol. 937, 2022, A19), to estimate unsteady fluctuations in the near wake of a NACA 0012 airfoil at $Ma = 0.3$, $Re = 5000$, and $\alpha = 6.5°$. The flow is simulated using direct numerical simulation, and global stability and resolvent analyses about the mean flow are performed to verify the accuracy of the linearization and elucidate the dominant flow physics. The resolvent-based estimators are obtained using two approaches: 1) an operator-based approach, resulting in low computational cost without the need for a priori model reduction, and 2) a data-driven approach that avoids building the linearized Navier-Stokes operator and statistically accounts for the nonlinearity of the flow. In both cases, a Wiener-Hopf formalism is used to optimally enforce causality. The resolvent-based estimators are then used to estimate unsteady fluctuations in the wake for the linear and nonlinear systems, which are forced by random upstream perturbations to break the periodic limit cycle produced by the vortex shedding and trigger chaotic fluctuations. The results demonstrate good accuracy in the near wake.

I. Introduction

Flow estimation is valuable in fluid mechanics for multiple purposes. First, it can be used to approximate the state of a flow at locations and/or for variables that cannot be directly measured or computed using as limited set of realizable measurements. Experimental equipment can be expensive for applications operating in extreme environments, such as high temperatures or pressure, e.g., high-speed aircraft or submarines, and avoiding such measurements can have significant benefits. Second, obtaining accurate and efficient estimators is crucial for achieving successful closed-loop control [1]. Accurate estimates of flow states provide the best feedback knowledge for a control system [2]. At the same time, it is challenging to build estimators computed efficiently from large-scale models due to high computational costs.

Meanwhile, airfoils at low Reynolds numbers ($Re_{L_c} < 10^4$) have received increased attention in recent years due to their relevance to low-speed/small-scale unmanned air vehicles (UAVs) [3]. While the relevant fluid dynamics at these low Reynolds numbers have been extensively studied [4–6], limited attention has been given to estimation and control [7, 8].

Taking account of the intimate relationship between estimation and control, classical estimation and control methods, which are Kalman filter [9], and Linear-quadratic-Gaussian control (LQG) combined with Kalman filter, respectively, have been noted in fluid mechanics over the last decade (Kalman filter:[10, 11], and LQG control:[12–16]). However, such a typical method contains two limitations, especially when they are applied to flows, such as aerodynamic flows, that require high-dimensional discretizations, e.g., many grid points. First, solving the Riccati equations required to obtain Kalman and LQG gains scales poorly with problem size and becomes computationally expensive or prohibitive for large systems. This can be partly mitigated by reducing the system a priori [17], but this potentially degrades the performance of the controller. Second, the classical methods cannot account for nonlinear terms of Navier-Stokes equations. As a result, it substantially deteriorates the estimation performance, in particular at high Reynolds numbers [18].

Resolvent analysis, also known as input-output analysis, is a methodology to investigate flow physics based on a linear mapping between response (output) and forcing (input) modes and the associated energetic gains in the frequency domain [19]. The leading resolvent modes have been shown to provide a useful approximation of coherent structures observed within the flow [20]. Recently, resolvent analysis has actively been leveraged for the interpretation of a NACA 0012 airfoil at different Reynolds numbers and angles of attack. Thomareis and Papadakis [21] performed resolvent analysis at $Re_{L_c} = 50,000$ and angle of attack 5° to study the physics of separated and attached flow over the airfoil. Symon *et al.* [22] investigated two angles of attack, 0° and 10°, of a NACA 0018 airfoil and showed that these two cases behave as an oscillator and amplifier [23], respectively. Yeh and Taira [24] used resovlent analysis

*Ph.D. student and AIAA student member
†Research fellow
‡Assistant professor and AIAA senior member

over a three-dimensional NACA 0012 airfoil at $Re_{L_c} = 23,000$, $Ma_\infty = 0.3$ and angle of attack 6° and 9° to design control input parameters for separation control. Kojima *et al.* [25] identified the origin of the two-dimensional transonic buffet over a NACA 0012 airfoil at $Re_{L_c} = 2,000$, $Ma_\infty = 0.85$ and $\alpha = 3°$ using resolvent analysis. Marquet *et al.* [26] also conducted resolvent analysis over a NACA 0012 $Re_{L_c} = 5,000$, $Ma_\infty = 0.3$ between $\alpha = 6.5°$ and $\alpha = 9°$, with an incompressible Navier-Stokes linear operator using the mean flow obtained from the numerical simulation and experimental results.

Recently, a resolvent-based approach was introduced to estimate space-time statistics and reconstruct time-series states using limited and non-causal measurements [18, 27]. More recently, the method was further extended to be available for building an optimal causal compensator with the enforcement of causality using Wiener-Hopf formalism so that it is applicable to a closed-loop flow control [28]. Unlike classical methods, resolvent-based approaches can statistically account for the nonlinear terms of the Navier-Stokes equations with colored-in-time correlations. Also, it allows for efficiently computing the large-scale linearized Navier-Stokes operator using an operator-based approach without any reduction of the system. This method was demonstrated over the backward-facing step flow with 96% of control performance in terms of perturbation energy reduction[29].

The present study aims to estimate unsteady fluctuations in the wake of a two-dimensional NACA 0012 airfoil at low Reynolds number *Re*=5,000 using resolvent-based tools [28]. The flow is computed via direct numerical simulation (DNS). As an initial step, we examine the global eigenmodes and resolvent modes to validate our linearized compressible Navier-Stokes operator and elucidate the key flow physics. The DNS results and eigenmodes are also validated against a previous study [26]. Next, non-causal and causal estimation kernels are built via operator-based and data-driven approaches. Finally, we demonstrate the estimation performance of our method for the linear system and nonlinear systems.

The remainder of this paper is organized as follows. In §II, we outline the methodology; the linear-time-invariant system is derived, and the resolvent operators are defined in II.A. Then, in II.B, three different estimation kernels are defined. We briefly show how an operator-based approach produces resolvent operators in II.C. Next, a data-driven approach is explained in II.D. In §III, the results for the simulation, global stability, resolvent analysis, and estimation are presented. Finally, the paper is summarized, and future work is discussed in §IV.

II. Methodology

A. System set-up

We start with the compressible Navier-Stokes equations written as

$$\frac{\partial \boldsymbol{q}}{\partial t} = \mathcal{F}(\boldsymbol{q}), \tag{1}$$

where $\boldsymbol{q}$ is a state vector of flow variables $[\rho, \rho u_x, \rho u_y, \rho u_z, \rho E]^T$ and $\mathcal{F}$ is the nonlinear Navier-Stokes operator. The equations are linearized using a Reynolds decomposition, giving

$$\frac{\partial \boldsymbol{q}'}{\partial t} - A\boldsymbol{q}' = \boldsymbol{f}(\bar{\boldsymbol{q}}, \boldsymbol{q}'), \tag{2}$$

where $\bar{\boldsymbol{q}}$ and $\boldsymbol{q}'$ represent the mean and perturbation state vectors of the flow variables, respectively. $\boldsymbol{A} = \frac{\partial \mathcal{F}(\bar{\boldsymbol{q}})}{\partial \boldsymbol{q}}$ is the linearized Navier-Stokes operator, and $\boldsymbol{f}$ consists the remaining nonlinear terms, including an external forcing. For convenience, we omit $(\cdot)'$ for perturbation from this point on.

To derive our estimation method, we consider a generalization of Eq. (2) in the form of the linear-time-invariant (LTI) system

$$\frac{d\boldsymbol{q}}{dt}(t) = \boldsymbol{A}\boldsymbol{q}(t) + \boldsymbol{B}_{\boldsymbol{f}}\boldsymbol{f}(t), \tag{3}$$

$$\boldsymbol{y}(t) = \boldsymbol{C}_{\boldsymbol{y}}\boldsymbol{q}(t) + \boldsymbol{n}(t), \tag{4}$$

$$z(t) = \boldsymbol{C}_{\boldsymbol{z}}\boldsymbol{q}(t), \tag{5}$$

where the forcing matrix $\boldsymbol{B}_{\boldsymbol{f}} \in \mathbb{R}^{\mathrm{n}\times\mathrm{n_f}}$ can be used to restrict the form of the forcing $\boldsymbol{f}$, and the measurement $\boldsymbol{y}$ and target $\boldsymbol{z}$ indicate readings of the state perturbation extracted by a measurement matrix $\boldsymbol{C}_{\boldsymbol{y}} \in \mathbb{R}^{\mathrm{n_y}\times\mathrm{n}}$ and a target matrix

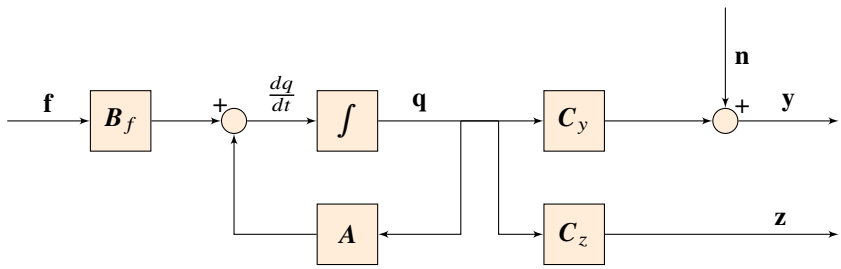

Fig. 1 Plant: linear system.

$\boldsymbol{C_z} \in \mathbb{R}^{n_z \times n}$. The number of the sensor and targets are denoted n_y and n_z, respectively. The vector $\boldsymbol{n}$ indicates the sensor noise. The LTI system is shown schematically in Fig. 1.

By Fourier-transforming the linear system into the frequency domain and defining a resolvent operator as $\boldsymbol{R} = (-\boldsymbol{A} - i\omega\boldsymbol{I})^{-1}$, we derive other resolvent operators that are used for building the resolvent-based kernels for estimation. The measurement and target vectors can be written as

$$\hat{\boldsymbol{y}} = \boldsymbol{R}_{y,f}\hat{\boldsymbol{f}} + \hat{\boldsymbol{n}}, \tag{6}$$

$$\hat{\boldsymbol{z}} = \boldsymbol{R}_{z,f}\hat{\boldsymbol{f}} \tag{7}$$

with $\boldsymbol{R_{y,f}} = \boldsymbol{C_y}\boldsymbol{R}\boldsymbol{B}_f$, $\boldsymbol{R_{z,f}} = \boldsymbol{C_z}\boldsymbol{R}\boldsymbol{B}_f$. The notation $(\hat{\cdot})$ reveals any quantity in the frequency domain in this study.

B. Resolvent-based estimation

We define three resolvent-based kernels for estimation: non-causal, truncated non-causal, and causal kernels. First, we start with a non-causal estimator using a convolution function, written as

$$\tilde{\boldsymbol{z}}_{nc}(t) = \int_{-\infty}^{\infty} \boldsymbol{T}_{z,nc}(t-\tau)\, \boldsymbol{y}(\tau) d\tau, \tag{8}$$

where $\boldsymbol{T}_{z,nc} \in \mathbb{R}^{n_z \times n_y}$ is a non-causal estimation kernel between the sensor measurement and the estimated target state with regard to the perturbation. To solve the estimation problem, a cost function is set up with an error between readings at a target and estimates, given by

$$\boldsymbol{J}_{nc}(t) = \int_{-\infty}^{\infty} \mathbb{E}\{e(t)^{\dagger} e(t)\}\, dt, \tag{9}$$

where the estimation error is defined as $e(t) = \boldsymbol{z}(t) - \tilde{\boldsymbol{z}}$. The operator $\mathbb{E}\{\cdot\}$ indicates an expectation in this study. By minimizing the cost function, we obtain a non-causal estimation kernel

$$\hat{\boldsymbol{T}}_{z,nc}(\omega) = \boldsymbol{R}_{z,f}\hat{\boldsymbol{F}}\boldsymbol{R}_{y,f}^{\dagger}(\boldsymbol{R}_{y,f}\hat{\boldsymbol{F}}\boldsymbol{R}_{y,f}^{\dagger} + \hat{\boldsymbol{N}})^{-1}, \tag{10}$$

where $\hat{\boldsymbol{F}} = \mathbb{E}\{\hat{\boldsymbol{f}}\hat{\boldsymbol{f}}^*\}$ and $\hat{\boldsymbol{N}} = \mathbb{E}\{\hat{\boldsymbol{n}}\hat{\boldsymbol{n}}^*\}$ denote the forcing covariance matrix and the sensor noise covariance matrix, respectively. The detailed derivation of the kernels is skipped in this paper. The readers can refer to Martini *et al.* [28].

Second, for real-time estimation, the input of the estimator is sensor measurements available only in the current and past. By enforcing the causality via Wiener-Hopf formalism in cost functions, we derive optimal causal estimation kernels under the constraint of causality. It allows integration of the convolution to evaluate only the casual part. A causal estimator

$$\tilde{\boldsymbol{z}}_{c}(t) = \int_{0}^{\infty} \boldsymbol{T}_{z,c}(t-\tau)\, \boldsymbol{y}(\tau) d\tau, \tag{11}$$

is defined in terms of the causal estimation kernel $\boldsymbol{T}_{z,c} \in \mathbb{R}^{n_z \times n_y}$. To enforce causality, we modify the cost function of Eq. (9) to read

$$\boldsymbol{J}_{c}(t) = \int_{-\infty}^{\infty} \mathbb{E}\{e(t)^* e(t)\} + (\boldsymbol{\Lambda}_{-}(t)\boldsymbol{T}_{z,c}(t) + \boldsymbol{\Lambda}_{-}^{\dagger}(t)\boldsymbol{T}_{z,c}^{\dagger}(t))\, dt, \tag{12}$$

where $\boldsymbol{\Lambda}$ is a Lagrange multiplier that is used for a constraint of the causal kernel to be zero for the non-causal part ($\tau < 0$). The non-causal and causal parts are defined as shown in Fig. 2. The subscript + and − represent the non-causal

($\tau < 0$) and causal ($\tau > 0$) parts of any matrix or function to be zero by achieving a Winer-Hopf factorization. The derived causal kernel for the estimation is

$$\hat{\boldsymbol{T}}_{z,c}(\omega) = (\boldsymbol{R}_{z,f}\hat{\boldsymbol{F}}\boldsymbol{R}_{y,f}^{\dagger}(\boldsymbol{R}_{y,f}\hat{\boldsymbol{F}}\boldsymbol{R}_{y,f}^{\dagger} + \hat{\boldsymbol{N}})_{-}^{-1})_{+}(\boldsymbol{R}_{y,f}\hat{\boldsymbol{F}}\boldsymbol{R}_{y,f}^{\dagger})_{+}^{-1}. \tag{13}$$

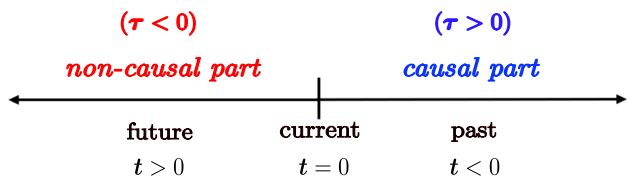

Fig. 2 Definition of the non-causal and causal parts in the convolution domain ($\tau = -t$).

For real-time estimation, the non-causal kernel is truncated at the current time by zeroing the non-causal part associated with unavailable future measurements. The truncated non-causal kernel is defined as

$$\boldsymbol{T}_{z,tnc}(\tau) = \begin{cases} \boldsymbol{T}_{z,nc}(\tau), & \tau \geq 0, \\ 0, & \tau < 0. \end{cases} \tag{14}$$

The truncated non-causal estimates are computed as

$$\tilde{z}_{tnc}(t) = \int_0^{\infty} \boldsymbol{T}_{z,tnc}(t-\tau)\, \boldsymbol{y}(\tau) d\tau. \tag{15}$$

C. Operator-based approach

The resolvent operator $\boldsymbol{R}$ is defined in terms of an inverse, which is computationally expensive to compute. For an airfoil grid, it is not feasible if we directly compute a resolvent operator. To overcome this issue, we employ a time-domain approach that avoids the inverse operation and instead builds the low-rank matrices needed to compute the estimation kernels [18, 28, 30]. The operator-based approach consists of multi-stage runs of the adjoint and direct linear equations. In this study, we apply a two-stage (adjoint-direct) run of the estimation system for the high-rank $\boldsymbol{B}_f$, and the low-rank $\boldsymbol{C}_y$ and $\boldsymbol{C}_z$. For more detail on the multi-stage runs, readers can refer to Martini *et al.* [28].

The procedure to build the estimation kernels begins with solving the adjoint system

$$-\frac{d\boldsymbol{q}_i}{dt}(t) = \boldsymbol{A}^{\dagger}\boldsymbol{q}_i(t) + \boldsymbol{C}_{y,i}^{\dagger}\delta(t), \tag{16}$$

$$\boldsymbol{s}_i(t) = \boldsymbol{B}_f^{\dagger}\boldsymbol{q}_i(t), \tag{17}$$

where $\delta(t)$ is a Dirac delta function used for an impulse forcing at the initial step, and the subscript i indicates the sensor defined by i-th row of the measurement matrix $\boldsymbol{C}_y$. The output of the adjoint run s_i is used as a forcing in a direct run. Check-pointing is used to reduce the memory requirements of saving snapshots of s_i from $O(N)$ to $O(2\sqrt{N})$, where N is the number of time steps. In the second stage, a direct equation is given by

$$\frac{d\boldsymbol{q}_i}{dt}(t) = \boldsymbol{A}\boldsymbol{q}_i(t) + \boldsymbol{B}_f\boldsymbol{s}_i(-t), \tag{18}$$

$$\boldsymbol{y}_i(t) = \boldsymbol{C}_y\boldsymbol{q}_i(t) + \boldsymbol{n}_i(t), \tag{19}$$

$$\boldsymbol{z}_i(t) = \boldsymbol{C}_z\boldsymbol{q}_i(t), \tag{20}$$

where $\boldsymbol{y}_i \in \mathbb{R}^{n_y \times 1}$ is a vector measured from all the sensors in the direct solution forced by i-th sensor, and $\boldsymbol{z}_i \in \mathbb{R}^{n_z \times 1}$ is a vector measured at all the targets in the direct solution forced by i-th sensor, which results in time-series low-rank matrices. By collecting the vectors of the i-th sensor and then Fourier-transforming, we obtain

$$\hat{\boldsymbol{Y}} = \begin{bmatrix} \hat{\boldsymbol{y}}_1 & \hat{\boldsymbol{y}}_2 & \dots & \hat{\boldsymbol{y}}_{n_y} \end{bmatrix} = \boldsymbol{R}_{y,f}\boldsymbol{R}_{y,f}^{\dagger}, \tag{21}$$

$$\hat{\boldsymbol{Z}} = \begin{bmatrix} \hat{\boldsymbol{z}}_1 & \hat{\boldsymbol{z}}_2 & \dots & \hat{\boldsymbol{z}}_{n_y} \end{bmatrix} = \boldsymbol{R}_{z,f}\boldsymbol{R}_{y,f}^{\dagger}, \tag{22}$$

with $\hat{\boldsymbol{Y}} \in \mathbb{C}^{n_y \times n_y}$ and $\hat{\boldsymbol{Z}} \in \mathbb{C}^{n_z \times n_y}$. That is, the y_i solutions of the adjoint-direct runs, for example, give the columns of the product [RHS of Eq. (21)]. The cost of this approach depends linearly on the problem dimension, avoiding the need to reduce the system via a priori model reduction and the associated loss of accuracy of the estimator.

As a result, the target non-causal and causal estimation kernels of Eq. (10) and Eq. (13) are computed by Eq. (21) and Eq. (22) obtained from the operator-based (O) approach with the assumption of white noise, given by

$$\hat{\boldsymbol{T}}_{z,nc,O}(\omega) = \hat{\boldsymbol{Z}}(\hat{\boldsymbol{Y}} + \hat{\boldsymbol{N}})^{-1}, \tag{23}$$

$$\hat{\boldsymbol{T}}_{z,c,O}(\omega) = (\hat{\boldsymbol{Z}}(\hat{\boldsymbol{Y}} + \hat{\boldsymbol{N}})_{-}^{-1})_{+}(\hat{\boldsymbol{Y}})_{+}^{-1}. \tag{24}$$

D. Data-driven approach

As an alternative to the operator-based approach, empirical cross-spectra densities (CSD) can be used to obtain the resolvent-based kernels, which is referred to as a data-driven approach [28]. When the CSD is computed from the dataset of a nonlinear system, it can statistically account for the nonlinearity of flow, which can improve estimation accuracy for the nonlinear system.

Following the notation of the LTI system in II.A, the datasets of the sensor and target readings are Fourier-transformed, then it can be expressed as

$$\begin{bmatrix} \hat{\boldsymbol{y}} \\ \hat{\boldsymbol{z}} \end{bmatrix} = \begin{bmatrix} \boldsymbol{R}_{y,f} & 1 \\ \boldsymbol{R}_{z,f} & 0 \end{bmatrix} \begin{bmatrix} \hat{\boldsymbol{f}} \\ \hat{\boldsymbol{n}} \end{bmatrix}. \tag{25}$$

Computing the cross-spectral density of $[\hat{\boldsymbol{y}} \quad \hat{\boldsymbol{z}}]^T$ using Eq. (25) gives

$$\begin{bmatrix} \boldsymbol{S}_{yf,yf} & \boldsymbol{S}_{yf,zf} \\ \boldsymbol{S}_{zf,yf} & \boldsymbol{S}_{zf,zf} \end{bmatrix} = \begin{bmatrix} \boldsymbol{R}_{y,f}\hat{\boldsymbol{F}}\boldsymbol{R}_{y,f}^{\dagger} & \boldsymbol{R}_{y,f}\hat{\boldsymbol{F}}\boldsymbol{R}_{z,f}^{\dagger} \\ \boldsymbol{R}_{z,f}\hat{\boldsymbol{F}}\boldsymbol{R}_{y,f}^{\dagger} & \boldsymbol{R}_{z,f}\hat{\boldsymbol{F}}\boldsymbol{R}_{z,f}^{\dagger} \end{bmatrix}, \tag{26}$$

with $\boldsymbol{S}_{yf,yf} = \mathbb{E}\{\hat{\boldsymbol{y}}\hat{\boldsymbol{y}}^*\}$ and $\boldsymbol{S}_{zf,yf} = \mathbb{E}\{\hat{\boldsymbol{z}}\hat{\boldsymbol{y}}^*\}$. Since the right-hand side of Eq. (26) contains the terms needed to build the estimation kernels, this shows that the correlations on the left-hand side can be used in their place. Note that the CSDs inherently contain statistical information about the nonlinearity of the flow within the forcing covariance matrix.

The non-causal and causal estimation kernels of Eq. (10) and Eq. (13) are computed by the CSDs of Eq. (26) resulting from the data-driven (D) approach, given by

$$\hat{\boldsymbol{T}}_{z,nc,D}(\omega) = \boldsymbol{S}_{zf,yf}(\boldsymbol{S}_{yf,yf} + \hat{\boldsymbol{N}})^{-1}, \tag{27}$$

$$\hat{\boldsymbol{T}}_{z,c,D}(\omega) = (\boldsymbol{S}_{zf,yf}(\boldsymbol{S}_{yf,yf} + \hat{\boldsymbol{N}})_{-}^{-1})_{+}(\boldsymbol{S}_{yf,yf})_{+}^{-1}. \tag{28}$$

III. Results

In this section, we begin by describing the problem setup and simulations as well as results from global stability and resolvent analyses used to validate our operators and elucidate the flow physics. Then, we demonstrate resolvent-based estimation for the linear system and nonlinear systems using operator-based and data-driven approaches.

A. Problem set-up and simulation

A direct numerical simulation using a high fidelity compressible flow solver CharLES, developed by Cascade Technologies, is used to simulate the flow around a NACA 0012 airfoil at low chord-based Reynolds number $Re_{L_c} = 5,000$ and the angles of attack $\alpha = 6.5°$. A C-shape mesh is created by Pointwise, as shown in Fig. 3 (a). In Fig. 3 (b), the computational grid near the airfoil is shown. The leading edge of the airfoil is located at the origin $x/L_c = y/L_c = 0$. The size in the streamwise and normal direction is $x/L_c \in [-49, 50]$, $y/L_c \in [-50, 50]$, respectively. The spanwise direction is extruded by only one step to be a planar 2D domain, which is $z/L_c \in [0, 0.1]$ using the symmetry boundary

conditions. A characteristic boundary condition for the farfield is used $[\rho, u_x, u_y, u_z, P] = [\rho_\infty, U_\infty, 0, 0, P_\infty]$, and the sponge layer is set as an outflow at $x/L_c \in [30, 50]$ with the running-averaged time $tU_\infty/L_c = 20$ to damp the reflected acoustic wave over the length of the sponge layer from the outflow boundary layer. For the time integration, a constant Courant-Friedrichs-Ley number is set to 1. In Fig. 3 (c), an instantaneous streamwise velocity field around the airfoil is presented. We can observe the vortex shedding in the wake and separation bubble over the airfoil.

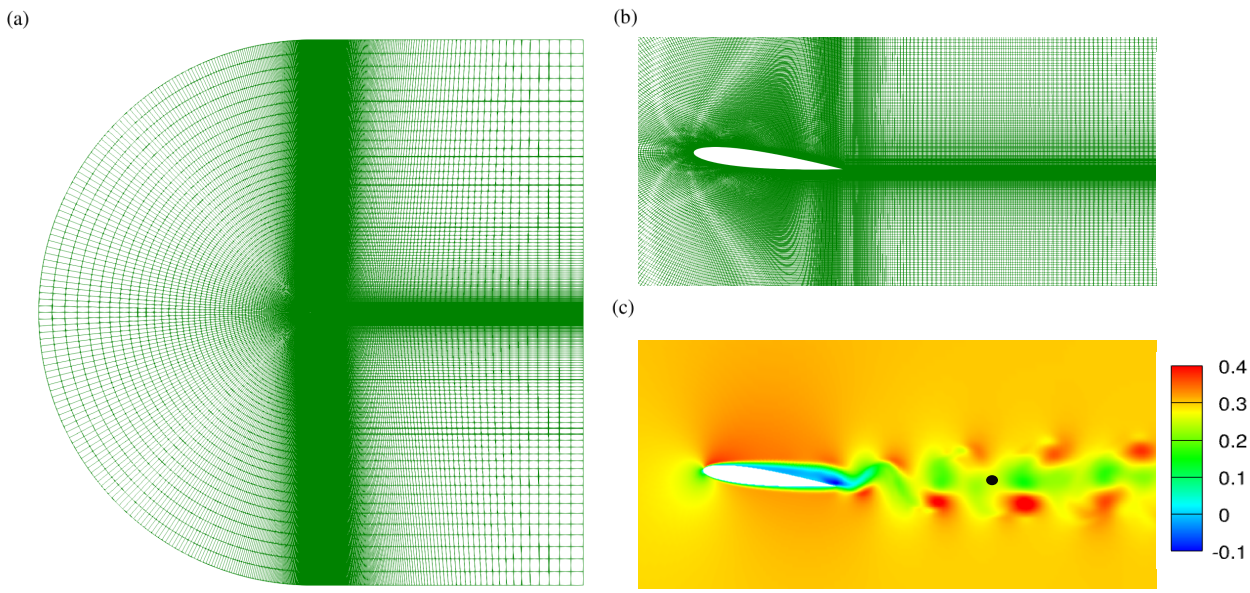

Fig. 3 Direct numerical simulation: (a) the full computational C-shape grid, (b) the close-up computational grid for the wall and wake regions, and (c) the instantaneous streamwise velocity ρu_x field using direct numerical simulation. The black dot is the probe location at $(x, y)/L_c = (2.1, -0.11)$ for the power spectral density in Fig. 4.

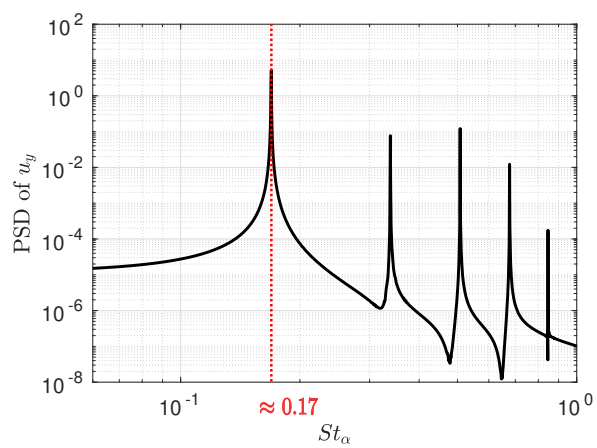

Fig. 4 Power spectral density (PSD) of the wall-normal velocity at $(x, y)/L_c = (2.1, -0.11)$.

We validate the DNS via comparisons of the vortex shedding frequency, aerodynamic forces, and vorticity field against the results of Marquet *et al.*[26], who considered incompressible flow over the same airfoil at the same Reynolds number and angle of attack. The probe to measure the wall-normal velocity is located at $x/L_c = 2.1, y/L_c = -0.11$. The vortex-shedding frequency $St_\alpha \equiv \omega_r(L_c sin\alpha)/(2\pi Ma_\infty)$ is found to be approximately 0.17 in the present study, shown as in Fig. 4, close to the value of 0.18 found by Marquet *et al.*. Next, the time-averaged drag and lift coefficients

over the surface of the airfoil are considered for validation. The drag and lift coefficients are

$$C_D = \frac{F_D}{\frac{1}{2}\rho_\infty U_\infty^2 A}, \quad \text{and} \quad C_L = \frac{F_L}{\frac{1}{2}\rho_\infty U_\infty^2 A}. \tag{29}$$

Table 1 shows that the present study matches the time-averaged drag and lift coefficient results of Marquet *et al.*[26] within a 2% tolerance. This slight difference could be the result of minor differences between the incompressible and compressible flow solutions or differences in the grid refinement; the present grid is more finely resolved.

	Marquet *et al.* [26]	Present study	Error
$\bar{C}_D$	0.088	0.0862	2.05%
$\bar{C}_L$	0.289	0.2941	1.76%

Table 1 The comparison of the time-averaged drag and lift coefficients at $\alpha = 6.5°$ with the results from incompressible periodic solution for a NACA 0012 airfoil at $Re_{L_c} = 5,000$ and $Ma_\infty = 0.3$.

Fig. 5 exhibits the vorticity field of the instantaneous and mean flow, which is similarly structured to the results obtained by Marquet *et al.*. We use the mean flow that time-averaged over $tU_\infty/L_c \in [0, 350]$ for the linearization work. The long window time allows for converging the vortex-shedding in the wake flow.

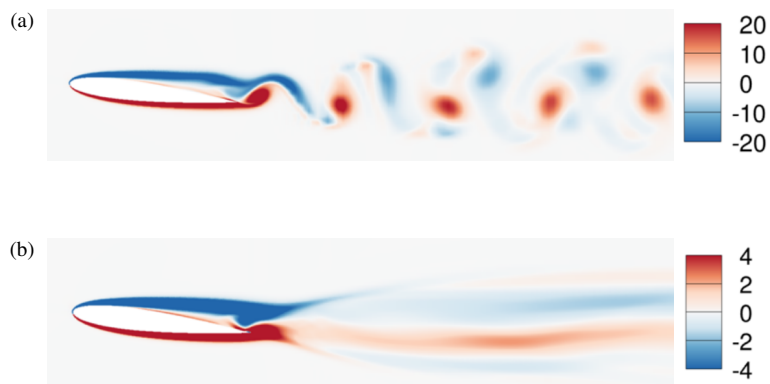

Fig. 5 Vorticity field of (a) the instantaneous flow, and (b) the mean flow.

B. Global stability

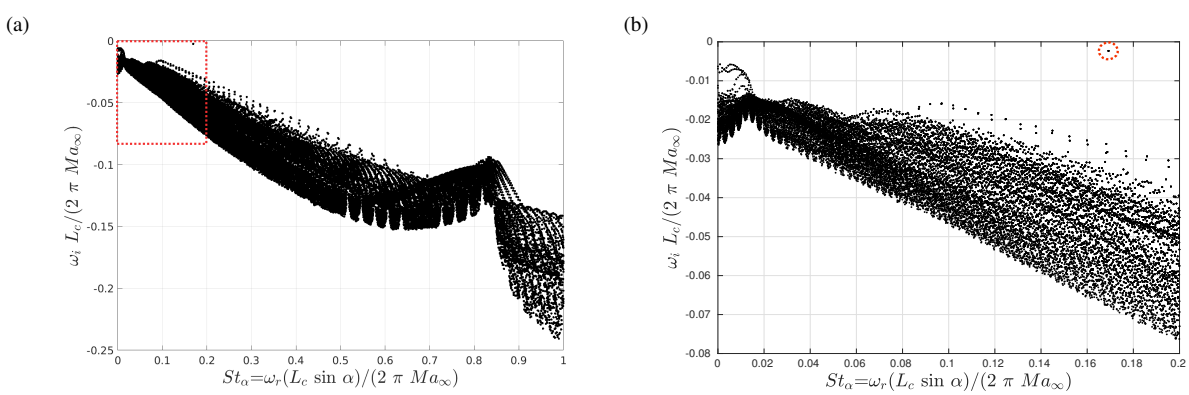

Fig. 6 Eigenspectrum: (a) overall eigenspectrum. The red box shows the bounds of (b), and (b) the close-up region of the eigenspectrum. The red circle is the dominant eigenmode at the vortex-shedding frequency $St_\alpha \approx 0.17$.

Resolvent-based estimation is nominally applicable and robust only for globally stable systems [31]. Thus, we first conduct a global stability analysis. Fig. 6 shows that all the values of the imaginary parts ω_i of the frequency, defined as $\lambda = -i\omega$, are below zero, indicating that the flow around the airfoil is globally stable. The dominant eigenmode at a vortex-shedding frequency in Fig. 6 exists at $St_\alpha \approx 0.17$, which corresponds to the result from PSD in Fig. 4. As we expected, the convective wake mode can be well observed from the eigenmodes, as shown in Fig. 7.

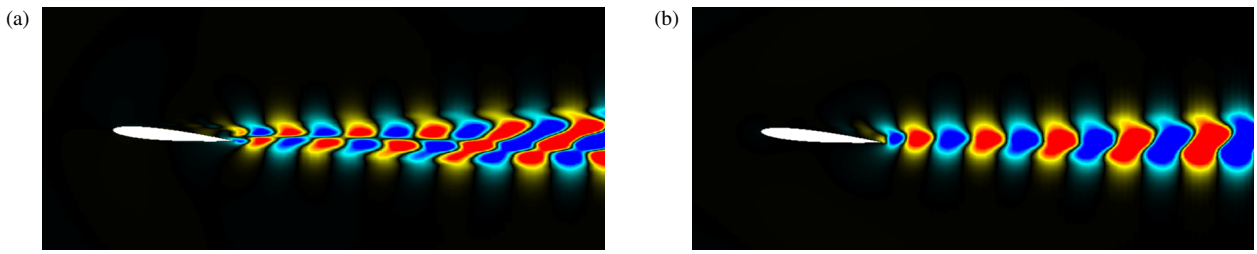

Fig. 7 Dominant eigenmodes at the vortex shedding frequency (red circle in Fig. 6-(b)): (a) streamwise velocity component ρu_x, and (b) wall-normal velocity component ρu_y.

C. Resolvent analysis

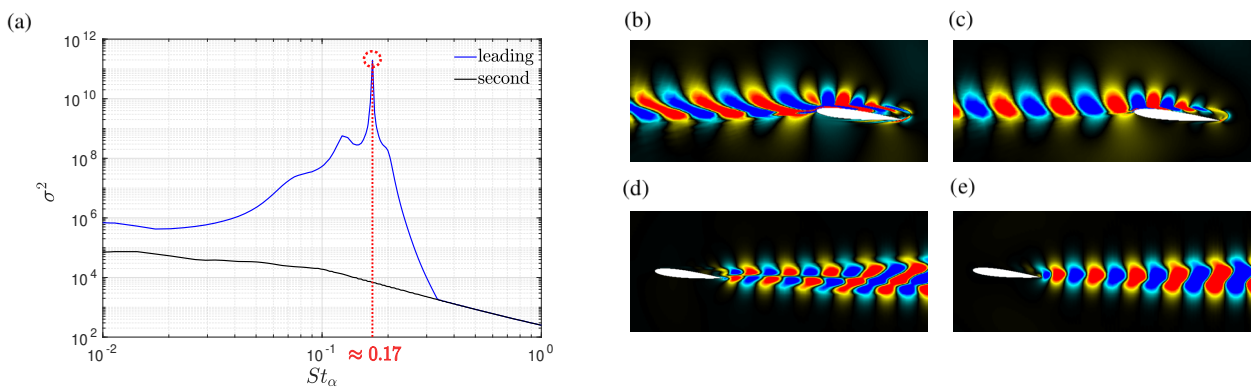

Fig. 8 Resolvent gains, optimal forcing and response modes: (a) leading and second optimal gains (red circle is expressed for the optimal resolvent modes (b),(c),(d),(e)), (b) optimal forcing mode of ρu_x, (c) optimal forcing mode of ρu_y, (d) optimal response mode of ρu_x, and (e) optimal response mode of ρu_y.

To obtain resolvent optimal gains and the corresponding forcing and response modes, we employ a modified resolvent operator

$$\tilde{R} = \boldsymbol{W}^{\frac{1}{2}}\boldsymbol{C}\boldsymbol{R}\boldsymbol{B}\boldsymbol{W}^{-\frac{1}{2}}. \tag{30}$$

where $\boldsymbol{C}$ and $\boldsymbol{B}$ are the identity matrix $\boldsymbol{I}$ in this work. The weight matrix $\boldsymbol{W}$ used for the norm [32] is defined as

$$\langle \boldsymbol{q}_1, \boldsymbol{q}_2 \rangle = \boldsymbol{q}_1^* diag\left(\frac{\bar{a}_0^2}{\bar{\rho}\gamma}, \bar{\rho}, \bar{\rho}, \bar{\rho}, \frac{\bar{\rho} c_v}{\bar{T}}\right)^T \boldsymbol{q}_2 = \boldsymbol{q}_1^* \boldsymbol{W} \boldsymbol{q}_2. \tag{31}$$

The resolvent gains are computed via the eigen-decomposition

$$\tilde{R}^*\tilde{R} = \boldsymbol{W}^{-\frac{1}{2}*}\boldsymbol{B}^*\boldsymbol{R}^*\boldsymbol{C}^*\boldsymbol{W}^{\frac{1}{2}*}\boldsymbol{W}^{\frac{1}{2}}\boldsymbol{C}\boldsymbol{R}\boldsymbol{B}\boldsymbol{W}^{-\frac{1}{2}} = \tilde{\boldsymbol{V}}\Sigma^2\tilde{\boldsymbol{V}}^*, \tag{32}$$

where $\Sigma = diag[\sigma_1, \sigma_2, ..., \sigma_{n_{freq}}]^T$, and σ_1 indicates the optimal resolvent gain. The action of R in Eq. (32) is obtained by computing its LU decomposition, and the eigenvalue problem is solved using Arnoldi iteration [33, 34]. The forcing and response modes can be recovered by $\boldsymbol{V} = \boldsymbol{W}^{-\frac{1}{2}}\tilde{\boldsymbol{V}}$ and $\boldsymbol{U} = \boldsymbol{W}^{-\frac{1}{2}}\tilde{\boldsymbol{U}}$.

In Fig. 8, the peak point of the leading resolvent gain is observed at the vortex shedding frequency $St_\alpha \approx 0.17$, which is dominant in this flow. The optimal forcing and response modes are shown in Fig. 8 (b)-(e). The optimal forcing mode is shaped upstream and over the airfoil, while the optimal response mode is well observed downstream in the wake. As the flow is convective from upstream, the input (forcing) and output (response) are located along the flow direction. The optimal response modes are similar to the dominant eigenmodes.

D. Resolvent-based estimation

As shown in the previous results in Fig. 6, 7, and 8, the flow is globally stable, and the resolvent analysis can explain the dominant physics of the airfoil, suggesting that a resolvent-based estimator will be effective. To make the problem more realistic, we add a random, zero-mean external forcing within a small region upstream of the airfoil to mimic free-stream noise (see Fig. 9 (a) and 14 (a)) for the linear and nonlinear system. This prevents the flow from falling into the periodic limit cycle associated with the vortex shedding process, yielding a chaotic flow instead.

For flow control in future work, the goal is to reduce the unsteady fluctuations beyond the trailing edge of the airfoil. The optimal sensor placement is beyond the scope of this paper, but physically, the sensor is likely located on the top surface of the airfoil. For these reasons, we place the sensor above the airfoil and the targets downstream in the near and far wake flow, as shown as in Fig. 9 (b) and 14 (b). Specifically, the sensor is at $[x/L_c, y/L_c] = [0.5, 0.1]$, and the targets are positioned at (a): $[x/L_c, y/L_c] = [0.6, 0.1]$, (b): $[0.9, 0.1]$, (c): $[1.2, 0.1]$, and (d): $[3.0, 0.1]$. This choice is also reasonable for control set-up in the amplifier flow [31].

1. Linear system

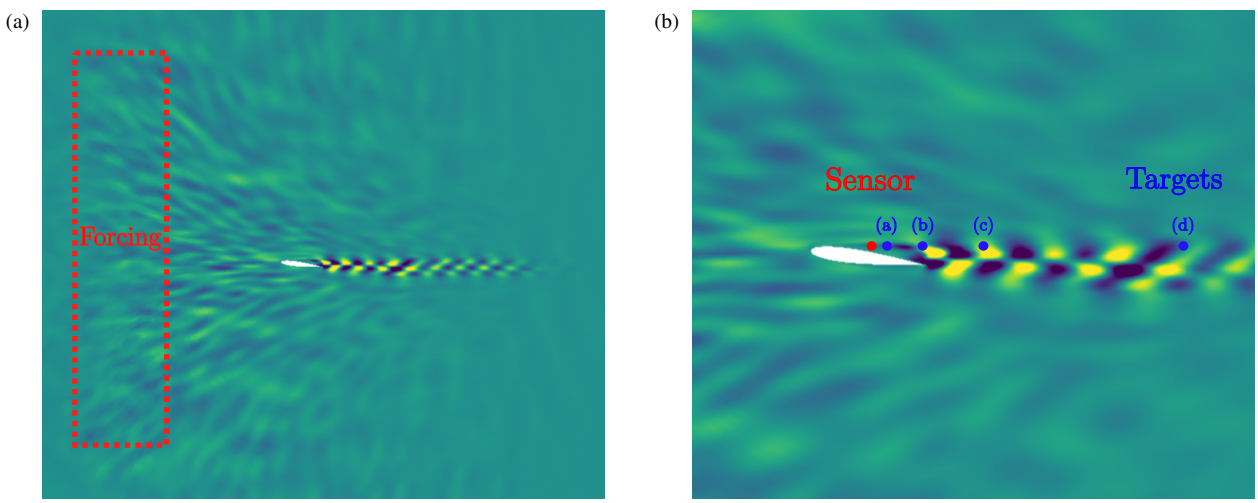

Fig. 9 The flow estimation setup for the linear system: (a) the instantaneous $\rho u_x'$ field from the linear system with the external forcing $x/L_c \in [-5, -3]$, $y/L_c \in [-5, 5]$, and (b) the sensor and targets setup in the $\rho u_x'$ field for estimation.

The two-stage runs are used to obtain the result of Eq. (21) and Eq. (22). To obtain the converged solution of the adjoint run, the total time is $tU_\infty/L_c \in [0, 24]$ and $\Delta t U_\infty/L_c$ is twice of the time step of DNS based on CFL number of 1. The reading interval of check-pointing is 96 of $\Delta t U_\infty/L_c$.

The non-causal part (future) can not be used for real-time estimation, so the truncated non-causal kernels are considered for flow estimation. The parameters for Wiener-Hopf factorization of the $\hat{Y}$ into $\hat{Y}_+$ and $\hat{Y}_-$, and the discretization of the kernels in the frequency domain are set to similar values as in the previous work [28].

All sensor and target readings are taken as averages over small spatial and temporal regions weighted by a Gaussian function in order to account for the finite size and resolution or real sensors and to ensure numerical convergence at finite grid resolution. The temporal support is $e^{-(t-t_0)^2\sigma_t}$ with $\sigma_t = 12.5$, and $t_0 = 1$, while the spatial support is $e^{-(x-x_c)^2/2\sigma_x^2-(y-y_c)^2/2\sigma_y^2}$ with $\sigma_x = 0.1$ and $\sigma_y = 0.05$. The sensor noise $\hat{N}$ is set to 10^{-2} of the maximum value of $\hat{Y}$. We identified that the sensor noise could affect the smoothness of the estimated data, but the amplitude of the output is not significantly affected.

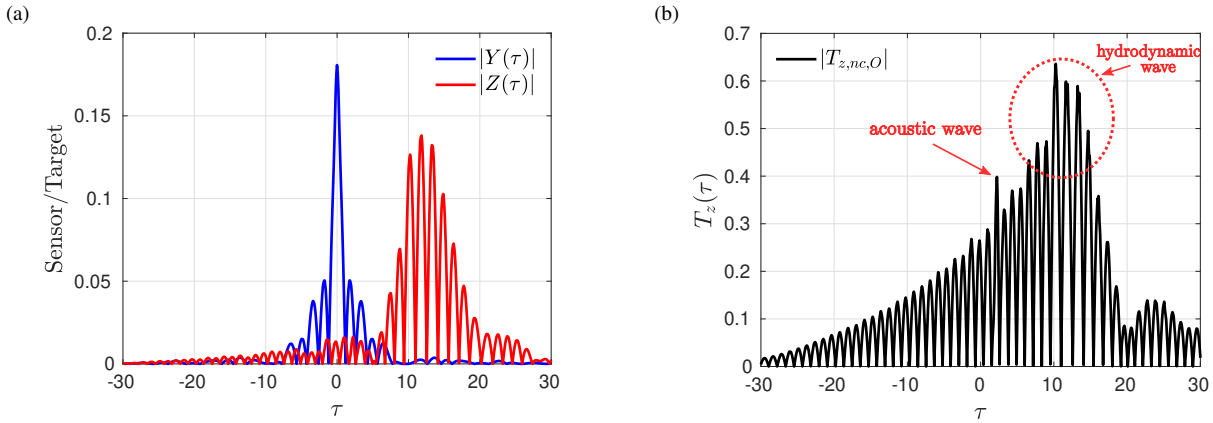

Fig. 10 Operator-based approach: (a) absolute solutions of the two-stage runs for the farthest downstream target $[x/L_c, y/L_c] = [3.0, 0.1]$, and (b) the absolute non-causal estimation kernel for the corresponding target.

Fig. 10 shows the results from the operator-based approach using a single sensor and a single target in the case of (d) ($[x/L_c, y/L_c] = [3.0, 0.1]$) in Fig. 9 (b). The sensor measurements in the direct run represent $Y(\tau)$, which has a distribution symmetric about $\tau = 0$ due to the impulse forcing at the initial step. Perturbations caused by the forcing $B_f s_i(\tau)$ travel downstream in the airfoil wake. Scattering perturbations occur near the trailing edge, which evolves a convective wave in the wake. Due to this physical phenomenon in the near wake, the target readings $\boldsymbol{Z}(\tau)$ in Fig. 10 (a) are a strong wave.

Due to the compressible effects, acoustic wave propagation is captured in the flow. As convective waves, hydrodynamic waves are observed. These two wave impacts have been reflected in the non-causal estimation kernel in Fig. 10 (b). Convection velocity near the shear layer in the wake is less than the free stream velocity. Therefore, the convection of hydrodynamic perturbations takes more time than the expected travel time to arrive at the target. The expected travel time for the distance $L/L_c = 2.5$ between the sensor and the target is $\tau = 8.3$ in the free stream ($Ma_\infty = 0.3$). Still, the convection in the wake of this flow takes around 80% slower than the free stream velocity due to the complex flow interaction, so the peak points of $\boldsymbol{T}_{z,nc,O}$ are broadly distributed around 10.41. The acoustic waves travel faster than the convection of hydrodynamic perturbations and also propagate upstream (feedback) and downstream. Thus, the peak point for the acoustic wave in the kernel is earlier positioned near $\tau = 2$, and the non-causal part can be explained by the acoustic wave feedback. That is, the non-causal estimation kernel includes this travel information between two points and produces the estimates from the sensor measurements.

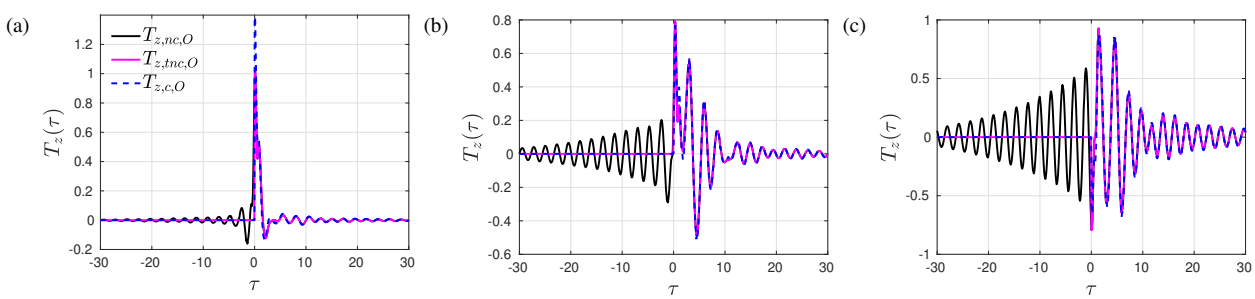

Fig. 11 Non-causal, truncated non-causal, and causal estimation kernels ($T_{z,nc,O}$, $T_{z,tnc,O}$, and $T_{z,c,O}$) using an operator-based (O) approach for the targets: (a) $[x/L_c, y/L_c] = [0.6, 0.1]$, (b) $[0.9, 0.1]$, and (c) $[1.2, 0.1]$ in Fig. 9 (b).

Non-casual (nc), truncated non-causal (tnc), and causal (c) estimation kernels for the three targets (a),(b), and (c) in Fig. 9 (b), computed using the operator-based approach, were shown in Fig. 11. The highest peak point of the non-causal kernels (and truncated non-causal) for three targets is moved to the positive τ ($\tau > 0$) direction as the target is located further downstream, as we expected. Also, the non-causal parts ($\tau < 0$) of the kernels are strong in the cases of the targets near the trailing edge (see Fig. 11 (b) and (c)), due to the strong scattering perturbation at the trailing edge.

The non-causal part of the kernel can come from the acoustic wave feedback, while the causal part is mostly caused by the convection of the hydrodynamic wave. As the acoustic wave feedback information is constrained on the causality, which is a relatively weak effect, the causal kernels that do not allow the non-causal part are similar to the truncated non-causal kernels, especially for the far downstream targets.

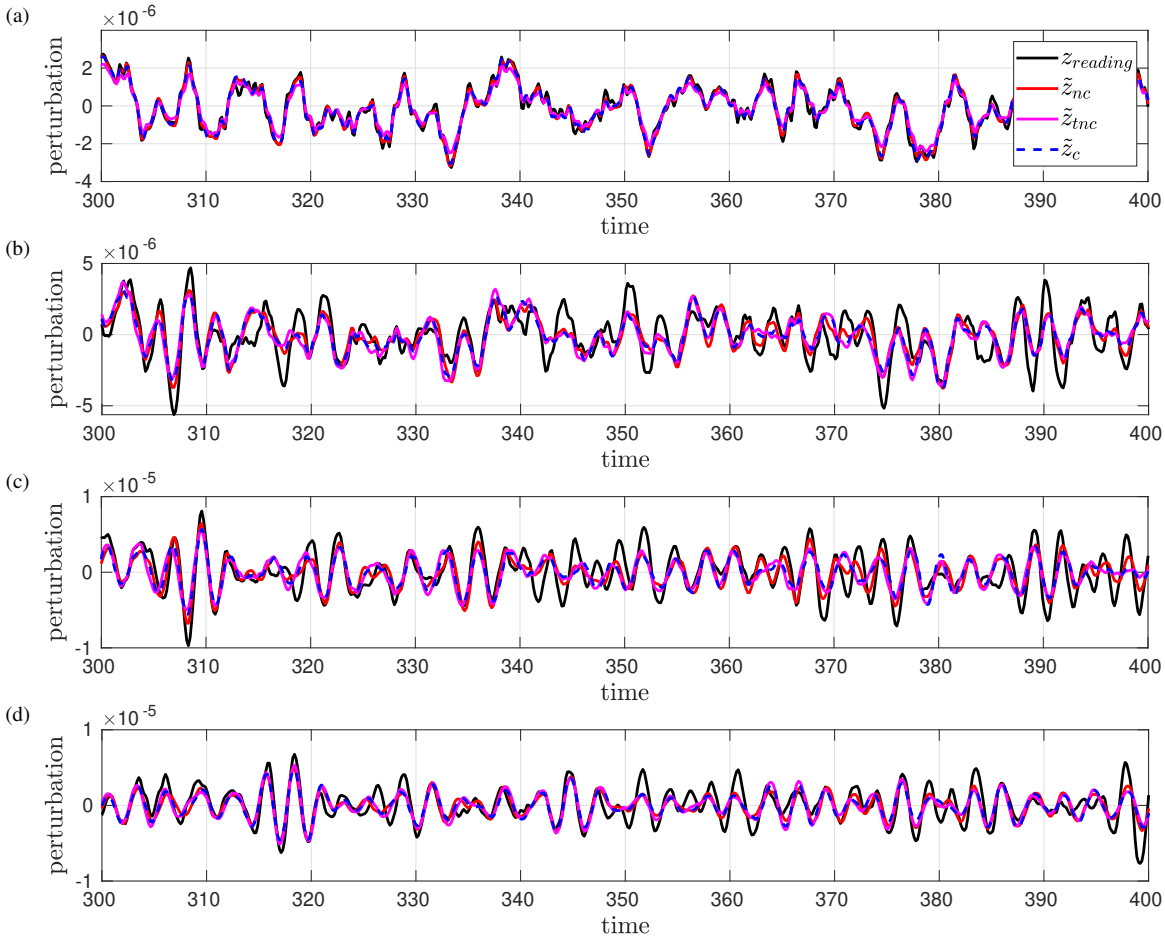

Fig. 12 Non-causal (nc), truncated non-causal (tnc), and causal (c) estimation using an operator-based approach for the linear system at the targets: (a) $[x/L_c, y/L_c] = [0.6, 0.1]$**, (b)** $[0.9, 0.1]$**, (c)** $[1.2, 0.1]$**, and (d)** $[3.0, 0.1]$ **in Fig. 9 (b).**

In Fig. 12, the non-causal, truncated non-causal, and causal estimation results are shown for the four target locations of (a), (b), (c), and (d) in Fig. 9 (b). All three methods produce accurate estimates. The accuracy decreases as the target moves downstream but remains reasonable even for the last target. The estimation error, which is defined as

$$Error = \frac{\Sigma_i \int (z_i(t) - \tilde{z}(t))^2 dt}{\Sigma_i \int (z_i(t))^2 dt}, \tag{33}$$

is shown as a function of the distance between the sensor and target L/L_c in Fig. 13. As expected, the non-causal estimator, which uses future information, provides the most accurate estimates. However, the causal estimation, which is optimal under the constraint on the causality, performs better than the truncated non-causal estimation, especially near the wave region. For the further downstream target, the estimation error is converged to around 0.4 in this work. The region where vortex shedding is strongly affected is less accurately estimated for the linear system.

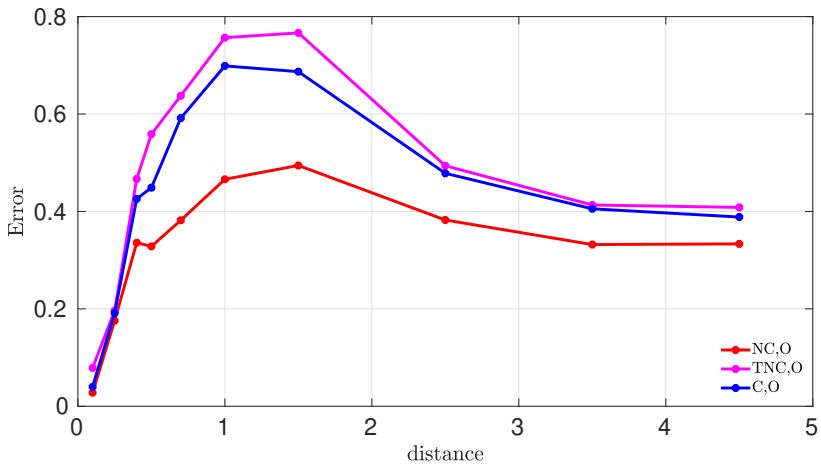

Fig. 13 Estimation error for the linear system as a function of the distance between the sensor and targets.

2. Nonlinear system

The flow is simulated using DNS with the same numerical setup as described earlier. The amplitude of the external forcing in the nonlinear system was set to $f_{amp} = 10^{-3}$, which was large enough to produce chaotic fluctuations in the wake. Since the estimator is defined in terms of perturbations to the mean, the mean is removed from the sensor readings before they are convolved with the estimation kernels.

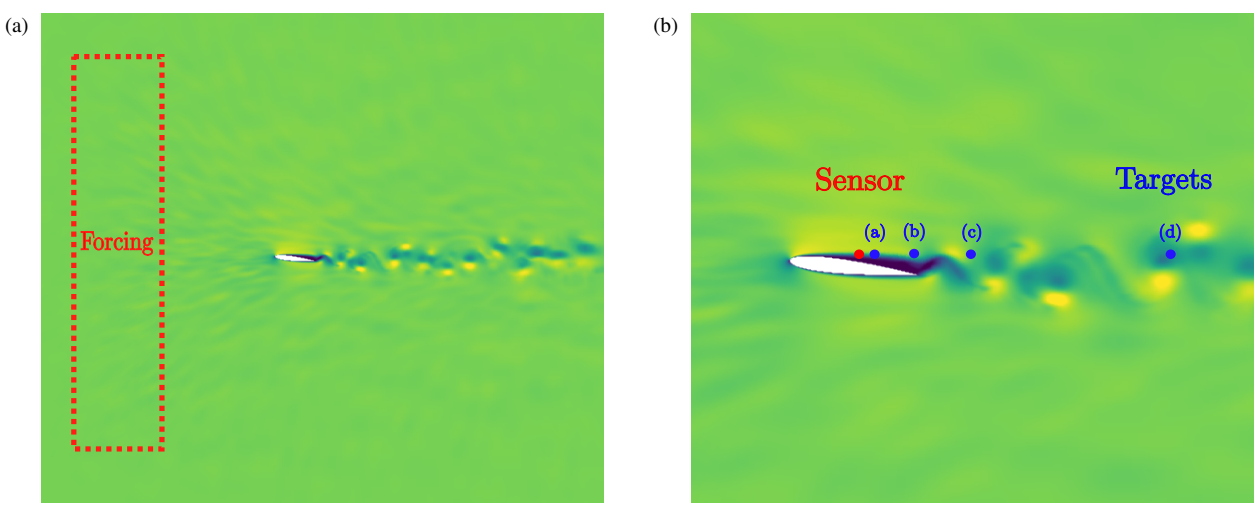

Fig. 14 The flow estimation setup for the nonlinear system: (a) the instantaneous ρu_x field of DNS with the external forcing $x/L_c \in [-5, -3]$, $y/L_c \in [-5, 5]$, and (b) the sensor and targets set-up in the ρu_x field for estimation.

Next, the estimation kernels obtained from the operator-based approach are applied to the nonlinear system. The estimates for the nonlinear system, shown in Fig. 15. are less accurate than those obtained for the linear system, shown in Fig. 12. This is increasingly apparent as the target is moved further downstream. Physically, this is explained by the increased opportunity for nonlinearity to influence the evolution of disturbances due to their greater travel time as the distance between the sensor and target increases. The causal and truncated non-causal estimators show similar performance for the nonlinear system.

Lastly, the data-driven kernels are used to estimate the nonlinear system. Eq.(26) derived in II.D is used to build the estimation kernels, which have the advantage over the operator-based kernels used in this study of statistically accounting for the nonlinearity of the flow. The data is collected from the direct numerical simulation, including the

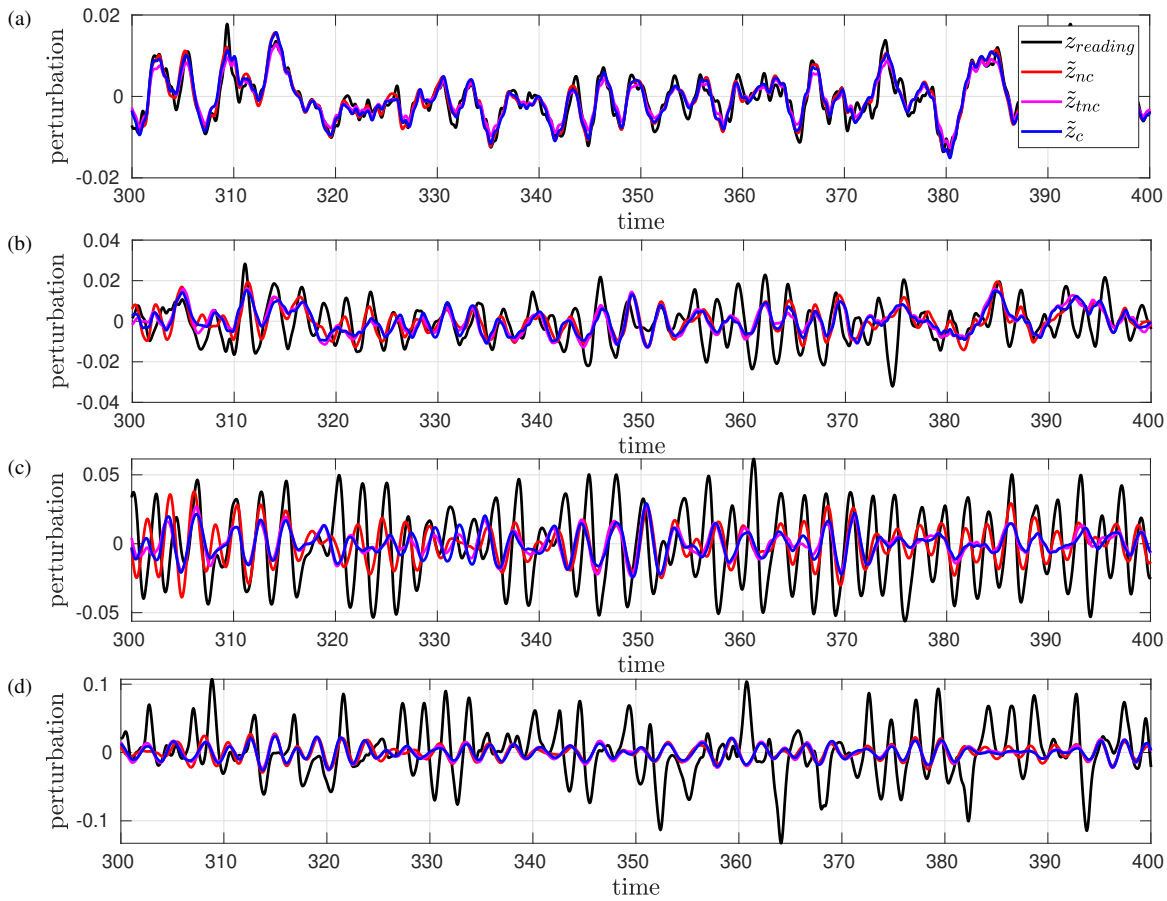

Fig. 15 Non-causal (nc), truncated non-causal (tnc), and causal (c) estimation using an operator-based approach for the nonlinear system at the targets: (a) $[x/L_c, y/L_c] = [0.6, 0.1]$**, (b)** $[0.9, 0.1]$**, (c)** $[1.2, 0.1]$**, and (d)** $[3.0, 0.1]$ **in Fig. 14 (b).**

external forcing. Welch's method [35] is used to obtain the CSD tensor needed to construct the data-driven kernel. The data is partitioned into 64 time windows of length $tU_\infty/L_c = 60$ with 50% overlap. Other parameters for building kernels and Wiener-Hopf factorization are the same as for the operator-based approach.

Fig. 16 shows the data-driven kernels computed from DNS data, which look similar to the operator-based kernels. The differences between the operator-based and data-driven kernels increase for targets further downstream. This is caused by the greater difference between the sensor and the target, which allows nonlinearity more opportunity to impact the evolution of disturbances. This impact is encoded within the data-driven kernels through their incorporation of the nonlinear forcing statistics, leading to differences in the kernels. In particular, the nonlinearity weakens the correlation between the sensor and downstream targets, leading to more emphasis on more recent data.

The inclusion of the nonlinear forcing color within the data-driven kernels improves the estimation results compared to the operator-based kernels, which assume white forcing, especially for the further downstream targets. The improvement can be observed by comparing Figs. 17 (data-driven) and 15 (operator-based). Fig. 18 reveals the estimation errors for the nonlinear systems using the operator-based and data-driven approaches. As expected, the estimation error increases as the distance between the sensor and the target increases. Also, in general, the data-driven approach outperforms the operator-based approach.

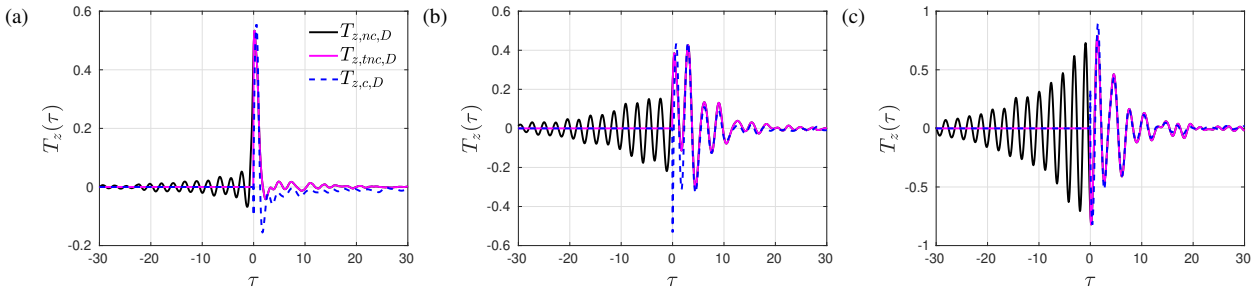

Fig. 16 Non-causal, truncated non-causal, and causal estimation kernels ($T_{z,nc,D}$, $T_{z,tnc,D}$, and $T_{z,c,D}$) using a data-driven (D) approach for the targets: (a) $[x/L_c, y/L_c] = [0.6, 0.1]$, (b) $[0.9, 0.1]$, and (c) $[1.2, 0.1]$ in Fig. 14 (b).

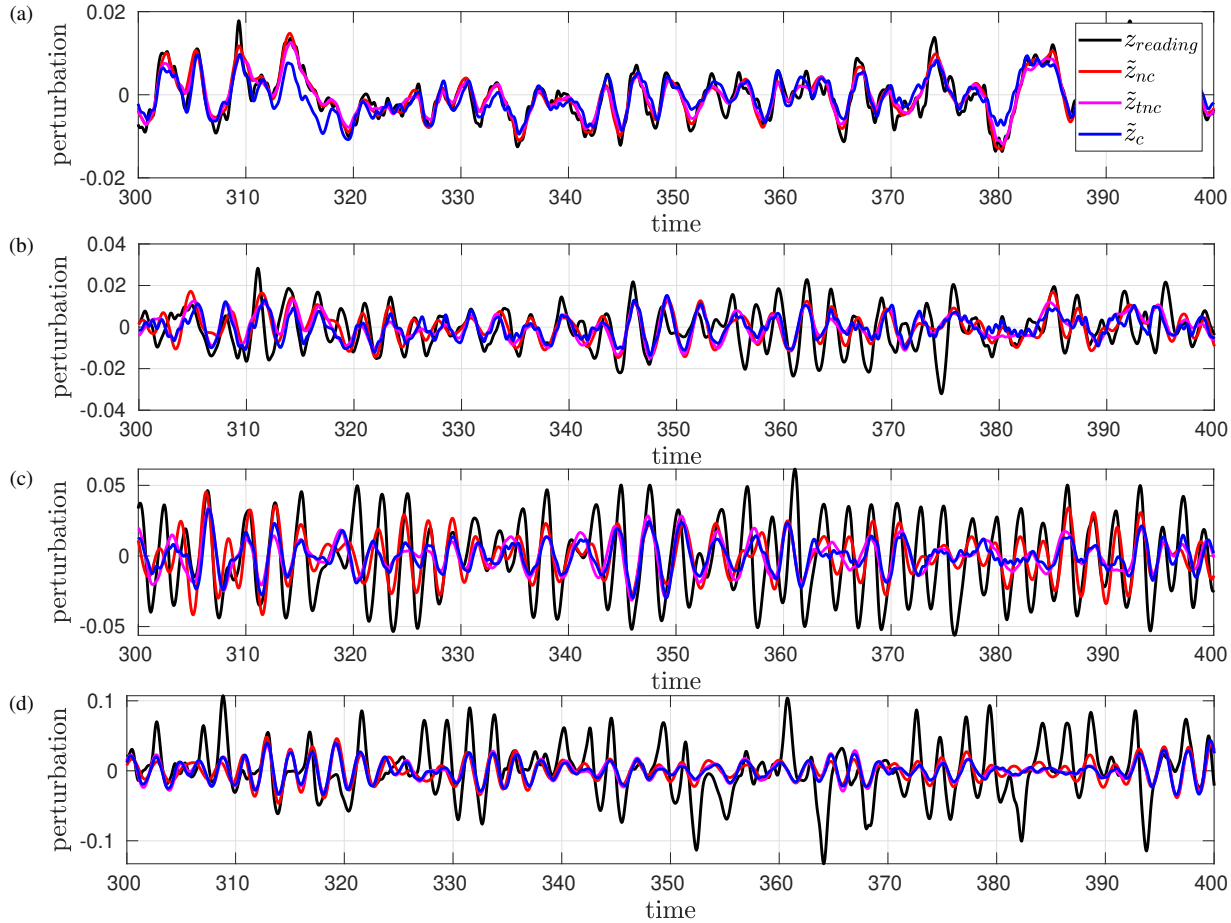

Fig. 17 Non-causal (nc), truncated non-causal (tnc), and causal (c) estimation using a data-driven approach for the nonlinear system at the targets: (a) $[x/L_c, y/L_c] = [0.6, 0.1]$, (b) $[0.9, 0.1]$, (c) $[1.2, 0.1]$, and (d) $[3.0, 0.1]$ in Fig. 14 (b)

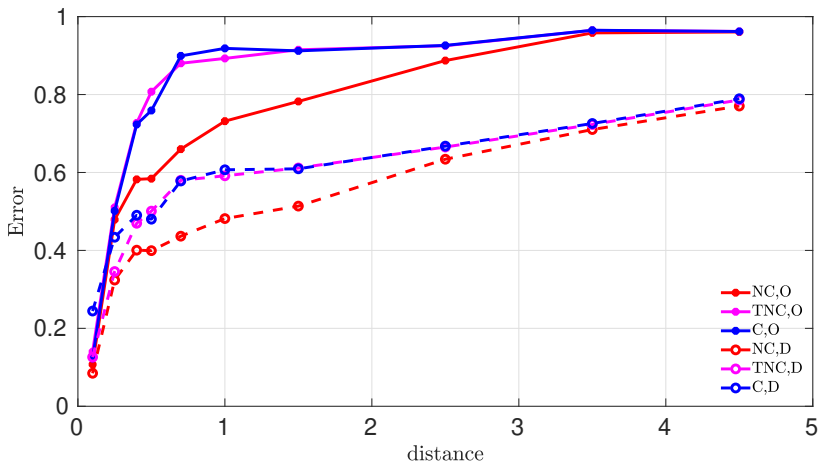

Fig. 18 Estimation error using the operator-based (O) and data-driven (D) approaches for the nonlinear systems as a function of the distance between the sensor and targets.

IV. Conclusion

In summary, we applied resolvent-based estimation to a two-dimensional NACA 0012 airfoil at $Ma = 0.3$, $Re = 5000$, and $\alpha = 6.5$ using operator-based and data-driven approaches. The resolvent-based framework is valuable in that we can build optimal estimation kernels with low-cost computation and statistically account for the nonlinearity of the flow. We demonstrated that the resolvent-based kernels can estimate the chaotic fluctuations, which are produced by external forcing, in the wake of the airfoil.

This work is ongoing. The estimation accuracy could be improved by using multiple sensors, leading to multiple-input multiple-output (MIMO) kernels, and by optimizing the sensor locations. The resolvent-based framework can naturally accommodate both of these improvements – the cost of building the kernels increases linearly with the number of sensors, and the performance of a given sensor arrangement can be estimated a priori, facilitating efficient optimization [28]. Additionally, the operator-based approach can include the forcing CSD, which is expected to bring its accuracy equal to or better than the data-driven approach.

As a next step, this resolvent-based estimation can be extended to closed-loop control. The estimated unsteady fluctuation around the mean flow can be used to compute the actuation signal, which can reduce the target fluctuations around the airfoil. Finally, we are working toward applying this approach to a three-dimensional turbulent airfoil flow at higher Reynolds numbers.

Acknowledgments

This research was supported by the Air Force Office of Scientific Research (AFOSR) under grant number FA9550-20-1-0214.

References

[1] Brunton, S. L., and Noack, B. R., "Closed-Loop Turbulence Control: Progress and Challenges," *Appl. Mech. Rev.*, Vol. 67, No. 5, 2015.

[2] Stengel, R. F., *Optimal Control and Estimation*, DOVER PUBLICATIONS, INC., 1994.

[3] Petricca, L., Ohlckers, P., and Grinde, C., "Micro- and Nano-Air Vehicles: State of the Art," *Intl. J. Aerospace Engineering*, Vol. 2011, 2011.

[4] Katz, J., and Plotkin, A., *Low-Speed Aerodynamics*, 2nd ed., Cambridge University Press, 2001.

[5] Huang, R. F., Wu, J. Y., Jeng, J. H., and Chen, R. C., "Surface flow and vortex shedding of an impulsively started wing," *J. Fluid Mech.*, Vol. 441, 2001, pp. 265–292.

[6] Wang, S., Zhou, Y., Alam, M. M., and Yang, H., "Turbulent intensity and Reynolds number effects on an airfoil at low Reynolds numbers," *Phys. Fluids*, Vol. 26, No. 11, 2014, p. 115107.

[7] Pasquale, L., Broglia, R., Choi, K.-S., Durante, D., and Zanchetta, P., "Robust control of flow separation over a pitching aerofoil using plasma actuators," *IFAC-PapersOnLine*, Vol. 50, No. 1, 2017, pp. 11120–11125.

[8] Broglia, R., Choi, K.-S., Houston, P., Pasquale, L., and Zanchetta, P., "Output feedback control of flow separation over an aerofoil using plasma actuators," *Intl. J. Numerical Analysis and Modeling*, Vol. 15, 2018.

[9] Kalman, R., "A new approach to linear filtering and prediction problems," *J. Basic Engng*, Vol. 82, 1960, pp. 35–45.

[10] Rafiee, M., Wu, Q., and Bayen, A. M., "Kalman filter based estimation of flow states in open channels using Lagrangian sensing," *Proceedings of the 48h IEEE Conference on Decision and Control (CDC)*, IEEE, 2009, pp. 8266–8271.

[11] Colburn, C. H., Cessna, J. B., and Bewley, T. R., "State estimation in wall-bounded flow systems. Part 3. The ensemble Kalman filter," *J. Fluid Mech.*, Vol. 682, 2011, pp. 289–303.

[12] Bagheri, S., Brandt, L., and Henningson, D. S., "Input–output analysis, model reduction and control of the flat-plate boundary layer," *J. Fluid Mech.*, Vol. 620, 2009, pp. 263–298.

[13] Fabbiane, N., Semeraro, O., Bagheri, S., and Henningson, D. S., "Adaptive and Model-Based Control Theory Applied to Convectively Unstable Flows," *Appl. Mech. Rev.*, Vol. 66, No. 6, 2014, p. 060801.

[14] Fabbiane, N., Simon, B., Fischer, F., Grundmann, S., Bagheri, S., and Henningson, D. S., "On the role of adaptivity for robust laminar flow control," *J. Fluid Mech.*, Vol. 767, 2015, p. R1.

[15] Fabbiane, N., Bagheri, S., and Henningson, D. S., "Energy efficiency and performance limitations of linear adaptive control for transition delay," *J. Fluid Mech.*, Vol. 810, 2017, pp. 60–81.

[16] Sasaki, K., Morra, P., Fabbiane, N., Cavalieri, A. V. G., Hanifi, A., and Henningson, D. S., "On the wave-cancelling nature of boundary layer flow control," *Theor. Comput. Fluid Dyn.*, Vol. 32, No. 5, 2018, pp. 593–616.

[17] Gomez, D. F., Lagor, F., Kirk, P. B., Lind, A., Jones, A. R., and Paley, D. A., "Unsteady DMD-Based Flow Field Estimation From Embedded Pressure Sensors in an Actuated Airfoil," *AIAA Scitech Forum*, 2019.

[18] Martini, E., Cavalieri, A. V. G., Jordan, P., Towne, A., and Lesshafft, L., "Resolvent-based optimal estimation of transitional and turbulent flows," *J. Fluid Mech.*, Vol. 900, 2020, p. A2.

[19] McKeon, B. J., and Sharma, A. S., "A critical-layer framework for turbulent pipe flow," *J. Fluid Mech.*, Vol. 658, 2010, pp. 336–382.

[20] Towne, A., Schmidt, O. T., and Colonius, T., "Spectral proper orthogonal decomposition and its relationship to dynamic mode decomposition and resolvent analysis," *J. Fluid Mech.*, Vol. 847, 2018, pp. 821–867.

[21] Thomareis, N., and Papadakis, G., "Resolvent analysis of separated and attached flows around an airfoil at transitional Reynolds number," *Phys. Rev. Fluids*, Vol. 3, No. 7, 2018, p. 073901.

[22] Symon, S., Sipp, D., and McKeon, B. J., "A tale of two airfoils: resolvent-based modelling of an oscillator versus an amplifier from an experimental mean," *J. Fluid Mech.*, Vol. 881, 2019, pp. 51–83.

[23] Huerre, P., and Monkewitz, P. A., "Local and Global Instabilities in Spatially Developing Flows," *Annu. Rev. Fluid Mech.*, 1990.

[24] Yeh, C., and Taira, K., "Resolvent-analysis-based design of airfoil separation control," *J. Fluid Mech.*, Vol. 867, 2019, pp. 572–610.

[25] Kojima, Y., Yeh, C., Taira, K., and Kameda, M., "Resolvent analysis on the origin of two-dimensional transonic buffet," *J. Fluid Mech.*, Vol. 885, 2020, p. R1.

[26] Marquet, O., Leontini, J., Zhao, J., and Thompson, M., "Hysteresis of two-dimensional flows around a NACA0012 airfoil at Re = 5000 and linear analyses of their mean flow." *Intl. J. Heat and Fluid Flow*, Vol. 94, 2022, p. 108920.

[27] Towne, A., Lozano-Durán, A., and Yang, X., "Resolvent-based estimation of space–time flow statistics," *J. Fluid Mech.*, Vol. 883, 2020, p. A17.

[28] Martini, E., Jung, J., Cavalieri, A., Jordan, P., and Towne, A., "Resolvent-based tools for optimal estimation and control via the Wiener–Hopf formalism," *J. Fluid Mech.*, Vol. 937, 2022, p. A19.

[29] Jung, J., Martini, E., Cavalieri, A., Jordan, P., Lesshafft, L., and Towne, A., "Optimal resolvent-based estimation for flow control," *APS Division of Fluid Dynamics*, Vol. G06, 2020, p. 004.

[30] Farghadan, A., Towne, A., Martini, E., and Cavalieri, A. V. G., "A randomized time-domain algorithm for efficiently computing resolvent modes," *AIAA Aviation Forum*, 2021.

[31] Schmid, P. J., and Sipp, D., "Linear control of oscillator and amplifier flows," *Phys. Fluids*, Vol. 1, No. 4, 2016, p. 040501.

[32] Chu, B.-T., "On the energy transfer to small disturbances in fluid flow (Part I)," *Acta Mechanica*, Vol. 1, No. 3, 1965, pp. 215–234.

[33] Jeun, J., Nichols, J. W., and Jovanović, M. R., "Input-output analysis of high-speed axisymmetric isothermal jet noise," *Phys. Fluids*, Vol. 28, No. 4, 2016, p. 047101.

[34] Schmidt, O. T., Towne, A., Rigas, G., Colonius, T., and Brès, G. A., "Spectral analysis of jet turbulence," *J. Fluid Mech.*, Vol. 855, 2018, pp. 953–982.

[35] Welch, P., "The use of fast Fourier transform for the estimation of power spectra: A method based on time averaging over short, modified periodograms," *IEEE Trans. Audio and Electroacoust.*, Vol. 15, No. 2, 1967, pp. 70–73.